# Chapitre 4

# uMan : A Low-Impedance Manipulator for Human-Robot Cooperation Based on Underactuated Redundancy

**Résumé**

Cet article revisite le concept de manipulateur sous-actionné afin d'améliorer significativement la coopération physique humain-robot (pHRI) pour l'industrie de l'assemblage. Le but principal, ici, est d'atteindre une manipulation fine qui soit intuitive et nécessitant un minimum d'effort peu importe le poids et la forme de la charge utile. Un manipulateur sous-actionné — dénommé uMan — basé sur une architecture macro-mini est donc conçu avec un nouveau mini mécanisme passif. Ce nouveau mini mécanisme passif a pour but de minimiser l'impédance effective, éliminer l'impédance non linéaire et découpler la dynamique de l'humain et la dynamique du robot. Une stratégie de commande est développée spécifiquement afin d'atteindre ces objectifs tout en considérant la nature sous-actionnée du robot pour la coopération et l'assistance autonome. Des validations expérimentales sont présentées et incluent une tâche d'insertion de goujon (peg-in-hole task) afin d'évaluer la facilité à produire des manipulations fines, une tâche de détection de collision afin de démontrer la sécurité du système et des tâches d'assemblage réelles afin d'établir la viabilité du concept en industrie.

## 4.1 Introduction

Humans are still essential to many industrial applications, because of their ability to intuitively adjust their interaction impedance depending on the task to be performed. However, certain tasks can be uncomfortable and exhausting while requiring human-fine manipulation capability.

This issue has motivated the emergence of different concepts of human-friendly robotic manipulators (Tadele et al. [2014]), notably, in the field of physical human-robot interactions (pHRI) (Krüger et al. [2009], Cherubini et al. [2016]). While these pHRI manipulators should alleviate the physical constraints on humans, they should as well increase fine manipulation performance.

In order to ensure effective fine manipulations, the main feature sought for intuitive pHRI manipulators is to perfectly match the human varying interaction impedance. This implies two specific criteria that a cooperative robot should follow, namely, *i*) minimizing the impedance and *ii*) eliminating the nonlinear impedance. Achieving these two fundamental objectives enables the human operator to deploy his/her own impedance, which naturally adapts to handling or assembly tasks. Due to the resulting low impedance, another important benefit of this fine manipulation objective is the increased safety during autonomous motion of the robot.

The prevalent approach to apparent impedance reduction in pHRI is the use of a force sensor in order to sense and regulate the operator's physical interaction. Using this force input, the actuated manipulator is thereby able to emulate different impedances. Such a technique is usually combined with an admittance controller (van der Linde and Lammertse [2003], Lecours et al. [2012]), a PI controller (Newman and Zhang [1994]), or even lead and lag compensators (Buerger and Hogan [2007]). However, it has been shown that the hardware dynamics limits the apparent impedance reduction (Hogan [1988]) and that any attempt to go below a certain fraction of the intrinsic inertia leads to unstable behaviours (Colgate and Hogan [1989]). Recent studies demonstrated that reduction ratios of 5 to 7 times the intrinsic inertia were feasible (van der Linde and Lammertse [2003], Buerger and Hogan [2007], Lecours et al. [2012]). Other approaches making use of force sensors include the appending of compliant material in order to mechanically filter the high-frequency interactions (Lamy et al. [2009]). Nevertheless, these large inertia reduction ratios are achievable only by overstepping the concept of passivity (Colgate and Hogan [1988], Colgate [1994]), which means that physical contacts are limited to specific ranges of environment dynamics.

In an industrial assembly context, where pHRI faces a broad range of environment dynamics, it is important to ensure passivity at all times as well as a fine and intuitive manipulation. Luckily, a common set of applications exist where the operational degrees of freedom (dof) can be permanently assigned to one of two spaces, namely the manipulative space and the constrained space. In the manipulative space, all the work — except for the gravity compensation forces — is performed by the human being, while in the constrained space, all the work is performed by the robot. Therefore, only the manipulative space needs to render the lowest possible impedance. Typical examples of such assembly applications are the ones involving lift assist devices. In fact, the most adequate solution is a collaborative manipulator using underactuated redundancy, which can passively provide a lower apparent impedance

than any actuated mechanism. Some mechanisms, such as cable-suspended intelligent assist devices (Wen et al. [2001], Campeau-Lecours et al. [2016]), already attempted to make use of this principle. Unfortunately, the handling of off-centred payloads and the ability to constrain rotational degrees of freedom are not possible with such cable-suspended devices.

It is thus proposed here to extend the principle of macro-mini manipulator using underactuated redundancy, presented in Labrecque et al. [2016], in order to provide intuitive and safe interaction yielding to very natural fine manipulation capabilities over a virtually unlimited workspace. This macro-mini concept includes high-impedance active (HIA) joints and low-impedance passive (LIP) joints, which have decoupled dynamics due to the mechanical redundancy. The HIA joints constitute the macro component — which is the portion attached to the fixed base — and are located outside of the human operator's workspace. The LIP joints constitute the mini component — which is the portion close to the end-effector — and are thus located in the manipulative space. Therefore, the HIA joints provide the payload handling capability by cancelling the forces applied by the human operator on the LIP joints, which leads to a low-impedance interaction.

The main contributions of this chapter to the field of pHRI are :
- A new design approach using a modified Chebyshev mechanism in order to increase the effective pendulum length for the horizontal LIP joints, while reducing their structural envelope size and weight as well as restraining all rotations.
- A two-mode statically balanced vertical motion using an extended compact version of the Sarrus mechanism.
- A unified control law that can transit between the autonomous and cooperative modes almost seamlessly due to the similar cooperative parameters for both modes.
- The introduction of a filtered parameter in the control law which improves the intuitiveness of the interaction.
- A novel collision detection that is specifically designed for this type of architecture and that considerably increases pHRI safety.

This chapter is structured as follows. Section 4.2 presents the mechanical architecture of the macro-mini underactuated manipulator (referred to as uMan) with an emphasis on the LIP joints and their advantages over other passive designs. Section 4.3 describes the control strategies and their implication for the cooperative mode and the autonomous mode as well as the highly efficient collision detection. Section 4.4 discusses the different experiments performed in order to validate the viability of the underactuacted manipulator in an industrial context. Finally, conclusions are drawn in the last section.

## 4.2 Active-Passive Mechanism

As mentioned above, an advanced assistive device using an active macro manipulator and a novel passive mini manipulator is presented in this chapter. From the previous work presented in Labrecque et al. [2016], it has been demonstrated that the passive mini manipulator must be capable of handling significant payloads, that the macro-mini mechanism should allow translations but constrain rotations, and that the end-effector should require minimal forces to be moved by the operator, i.e., low impedance, but should passively return to its central reference configuration when no external force is applied. These objectives have thus driven the design of the new mini mechanism in addition to the new objectives which are : the extension to a 3-dof mechanism and the reduction of its total weight and size. It is noted that the extension to a 3-dof mechanism is not trivial since the added dof corresponds to the vertical translation, which must support the weight of the payload. A number of concepts have thus been investigated for their suitability to act as passive mini mechanisms and the main results of this investigation are reported in this section.

### 4.2.1 Passive horizontal motion

A first possible strategy for the structure of the mini is the use of three linear rails orthogonally stacked in series, including vertical motion. Industrial rails can support large payloads and are relatively compact. Unlike the passive manipulator presented in Irino et al. [2013], here, springs are required in order to passively return the mechanism to its central position. Unfortunately, friction in the linear rails increases significantly with offset payloads. Because of this friction, the return force must be significant which yields a large deadband at the central position. As a result, the interaction is neither intuitive nor comfortable for the user.

A second strategy is to use parallelograms for the two horizontal degrees of freedom. The use of parallelograms considerably reduces friction — due to the use of revolute joints instead of rails — and makes it possible to use gravity to passively returning the mechanism to its central position due to the inherent pendulum motion. Parallelogram four-bar mechanisms also maintain the orientation of the end-effector and allow off-centred payloads. This approach is compared with the state-of-the-art admittance control in Labrecque et al. [2016] and is shown to lead to significant effective impedance reduction at the end-effector (for more details, see Section 4.7.2). However, parallelogram mechanisms also have drawbacks such as the vertical parasitic motion and the magnitude of the return force that increases with the weight of the payload. Indeed, when the coupler link of a parallelogram mounted in a vertical plane is moved horizontally, a vertical parasitic motion is induced, which means that the payload is moved up, thereby requiring a significant force — proportional to the weight of the payload — from the human user. One way to reduce this effect is to increase the length of the equivalent pendulum, but unfortunately this leads to an increase of the parallelogram's link lengths which then results in a bulky mechanism.

An alternative strategy, in order to increase the effective length of the pendulum motion and obtain a more compact mechanism with reduced weight and size, is to use straight-line mechanisms based on revolute joints. Straight-line mechanisms produce a straight-line (or an approximate straight-line) motion of a specific point on one of the links of their coupler over a given range of motion of the joints. By slightly modifying the geometry of such mechanisms, motion trajectories with a large radius of curvature can be obtained with relatively short links, thereby allowing gravity to return the mechanism to its central configuration, without requiring large forces from the human operator. Several straight-line mechanisms can be found in the literature (Chironis [1991]), but the four-bar Chebyshev mechanism (Chironis [1991]) is selected in this work due to its inherent structural robustness.

The Chebyshev mechanism is therefore modified in order to obtain a radius of curvature three times larger than the length of the crank links, as depicted in Fig. 4.1 which significantly reduces the vertical parasitic motion and thereby the effective impedance. Furthermore, in order to constrain the rotation around an axis normal to the plane of the mechanism, two four-bar mechanisms are mounted in parallel between the base and the end-effector. The resulting modified double Chebyshev mechanism, referred to as Large Radius Chebyshev Parallelogram (LRCP), is shown in Fig. 4.2. In practice two parallel mechanisms mounted in parallel planes are linked together by structural bars in order to withstand the moments along the other axes as illustrated in Fig. 4.3 for the two horizontal motions.

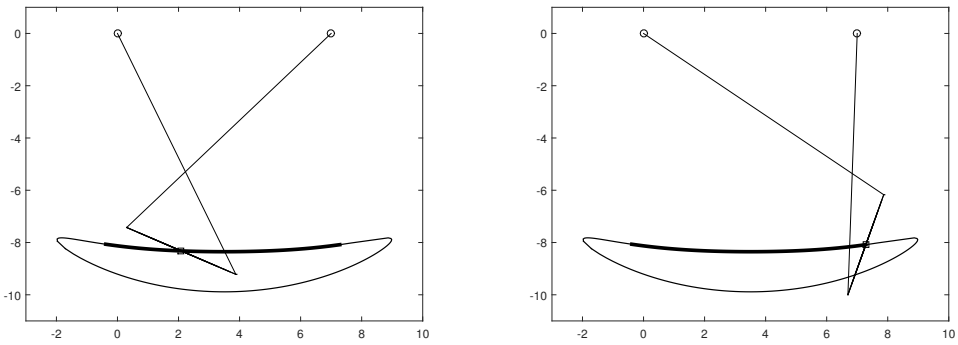


FIGURE 4.1 – Two configurations of a modified Chebyshev mechanism with the path traced by the centre of the coupler. The upper portion of the path approximately describes a circular arc with a large radius of curvature. The bold section of the coupler curve corresponds to the range of motion that can be used in practice.

### 4.2.2 Passive vertical motion

The concept used for the horizontal LIP joints, namely the LRCP, cannot be directly applied to a vertical motion since gravitational forces tend to pull the mechanism downwards, eliminating the possibility for the mini mechanism to have a bidirectional range of motion. A different concept is therefore developed for the vertical motion of the mini mechanism.

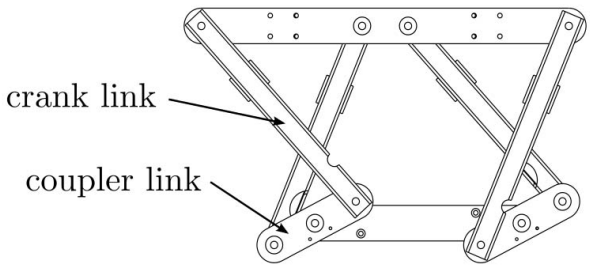


FIGURE 4.2 – Large Radius Chebyshev Parallelogram, comprising two modified straight-line Chebyshev mechanisms connected by a coupler link.

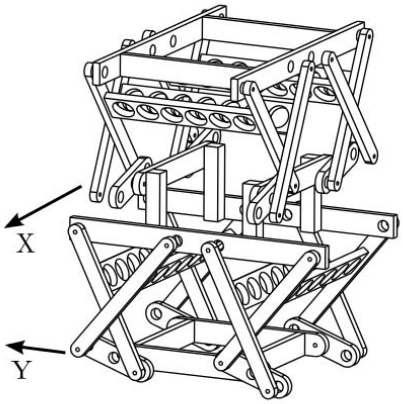


FIGURE 4.3 – CAD model of the LRCP mechanisms producing pendulum-type parallelogram motions in both horizontal directions, with a large radius of curvature.

In order to obtain a behaviour similar to that described above for the horizontal motion, it is required to have the minimum potential energy in the desired centre of the mechanism's range of motion. In other words, the dynamics of gravitational forces acting on a pendulum must be reproduced but for a vertical motion. With a careful design using the potential energy stored in a spring one can counterbalance the variation of gravitational potential energy while the system moves, thereby creating a virtual pendulum dynamics. In order to produce an effective human-robot interaction, such a design should be capable of performing a pure translation using only rotational joints and be capable of withstanding moments. The concept of the Sarrus linkage (Hunt [1967]), shown in Fig. 4.4, is therefore used for the design of the new vertical LIP joint.

An extension spring is attached from the base to the first link, as depicted in the complete mechanism shown in Fig. 4.5. The spring is selected in order to optimize the range of motion of a specific payload's weight, i.e., having the minimum potential energy in the centre of the proposed Sarrus mechanism's range of motion. However, in a practical application, the mechanism should be able to operate in two modes, namely loaded and unloaded, which

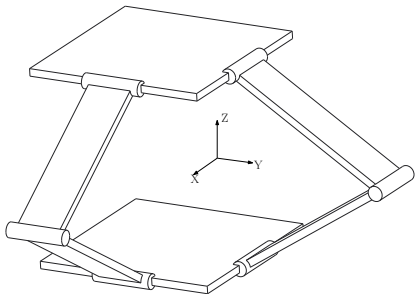


FIGURE 4.4 – Sarrus linkage : two orthogonal sets of three revolute joints with parallel axes are connecting two moving bodies, thereby producing a constraint equivalent to a prismatic joint between these bodies.

thereby requires two different static balancing systems. When the device is loaded (Fig. 4.2.2), the payload and the mechanism are balanced by the extension spring, with the equilibrium position in the centre of the vertical range of motion, thereby allowing intuitive manipulation of the payload by the human user. On the other hand, when no payload is attached to the mini mechanism (unloaded state, Fig. 4.2.2) the end-effector of the Sarrus linkage moves up — due to the effect of the extension spring — and presses against a mechanical stopper. This stopper is coupled with a compression spring (shown in Fig. 4.5) and allows the operator to interact with the end-effector of the unloaded device, within a small range of vertical motion. It is recalled that the main objective of the uMan robot is to assist the user with the payload manipulation, for which low impedance interaction is provided including in the vertical direction, based on the gravity compensation system described above. When the device is unloaded, the compression spring provides interaction capabilities, although with higher impedance and smaller range of motion. This is not critical for typical industrial applications because the unloaded state is mainly used to teach the robot where to pick-up and drop the payloads, which should be needed only sporadically. The compression spring also acts as a safety switch when the unloaded robot is moving autonomously.

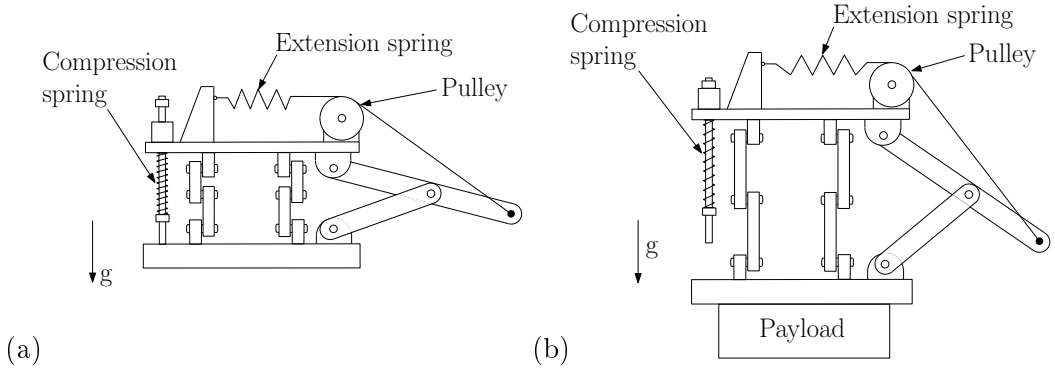


FIGURE 4.5 – The two states of the Sarrus mechanism. (a) Unloaded state (b) Loaded state.

### 4.2.3 Active macro manipulator

The active macro manipulator used in this work is a gantry robot that provides the three translational degrees of freedom over a large workspace. This component of the manipulator was designed for large payloads and has an equivalent moving mass of 500 kg in the $x$-direction and of 350 kg in the $y$-direction. Its architecture is described in detail in Gosselin et al. [2013]. Here, the suspended bridge architecture is also favoured because of its prevalence in the assembly industry. The prototype of the macro-mini uMan is shown in Fig. 4.6.

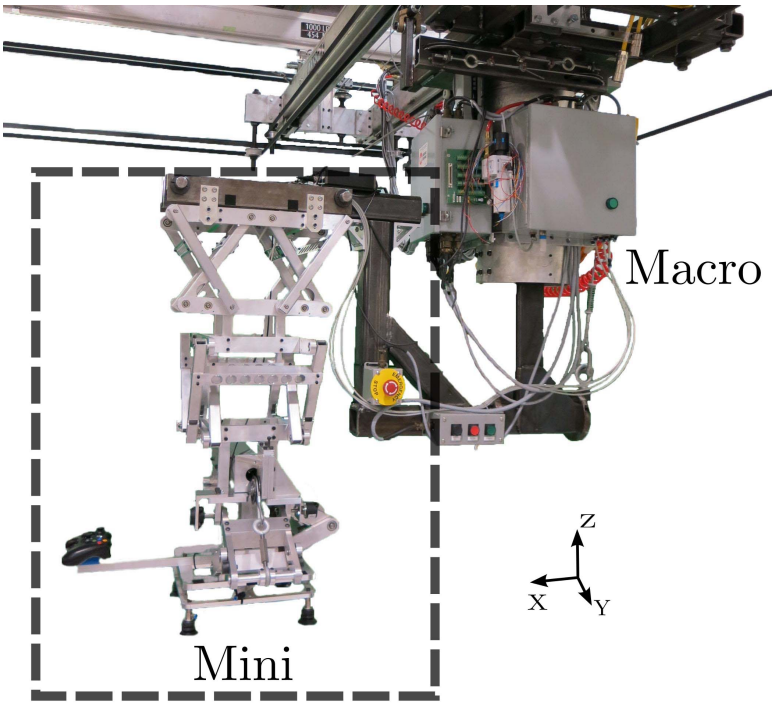


FIGURE 4.6 – Macro-mini uMan. Macro : 3-dof gantry manipulator. Mini : 3-dof passive mechanism.

## 4.3 Control of the active-passive mechanism

If the macro-mini manipulator described in Section 4.2 is designed properly following the system's requirements, then the necessary controller can be rather simple. Indeed, the resulting dynamics is equivalent to that of a moving cart with a suspended pendulum. However, the main objective of the uMan is to provide an intuitive and safe interaction between the operator and the robot. Therefore, besides the addition of a safe autonomous mode, the controller has to accommodate certain comfort aspects such as a reduction of the impedance felt by the operator, a reduction of the required force to maintain its velocity, and a quick and intuitive reaction to unexpected contacts. These specific physical human-robot interaction (pHRI) aspects are considered in the novel control law which thereby includes additional functionalities such as a unique control law for both modes, namely autonomous and cooperative, a new intui-

tive filtered parameter, and a highly efficient collision detection. The controller comprises two main control loops, namely the inner control loop for the motor input and the outer control loop for the external input. Both control loops are described in detail in the next subsections.

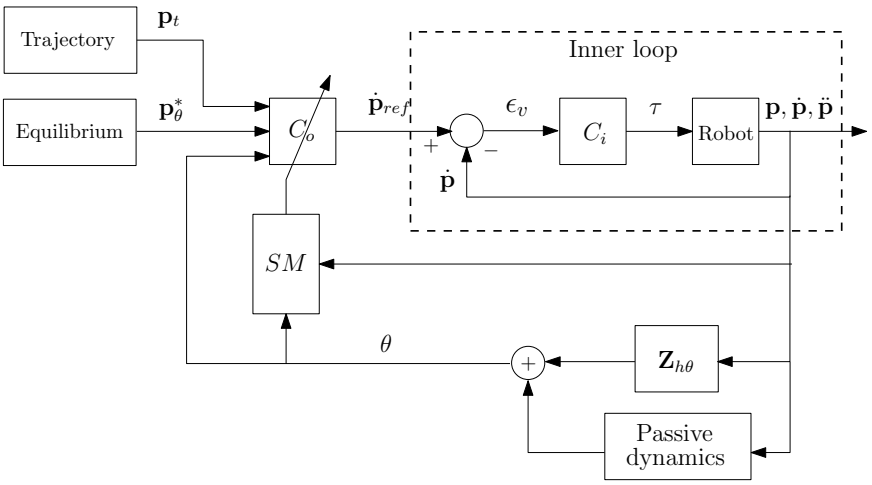


FIGURE 4.7 – Control architecture for the active-passive uMan.

### 4.3.1 Inner control loop

The internal control, $C_i$, is performed at the macro manipulator's joint level with a proportional velocity regulation. A compensation of the dry friction, $\boldsymbol{\tau}_f$, is also added at the torque level in order to reduce the mechanical delay, leading to

$$\boldsymbol{\tau} = \mathbf{K}_p \boldsymbol{\epsilon}_v + \boldsymbol{\tau}_f \tag{4.1}$$

where $\boldsymbol{\tau}$ is the array of input torque for the macro manipulator's actuators, $\mathbf{K}_p$ is the diagonal proportional gain matrix and $\boldsymbol{\epsilon}_v = (\dot{\mathbf{p}}_{ref} - \dot{\mathbf{p}})$ is the array of velocity error as depicted in Fig. 4.7.

The nature of the interaction, i.e., a human user and a passive compliance at the end-effector, allows the use of such a simple inner control loop. However, if a high positioning accuracy is required when the robot is operating in autonomous mode, an inverse dynamics control with a position regulation could be more appropriate.

### 4.3.2 Outer control loop

The global control is performed in the end-effector's Cartesian space and includes a general controller with specific parameters depending on the operation mode. As mentioned above, the two main modes of operation are the autonomous mode and the cooperative mode. For each of these modes, the cases with and without payload are included. A state machine, represented

by the *SM* block in Fig. 4.7, enables the mode switch according to the current and desired state of the manipulator. Moreover, a vector representing the position of a reference point on the end-effector of the mini manipulator with respect to a reference point on the end-effector of the macro manipulator is defined as $\mathbf{p}_\theta$, which is a function of the (passive) joint coordinates of the LIP joints of the mini manipulator. Also, the array of LIP joint coordinates is defined as

$$\boldsymbol{\theta} = \begin{bmatrix} \theta_x & \theta_y & \theta_z \end{bmatrix}^T$$

where $\theta_x$, $\theta_y$ and $\theta_z$ are respectively associated with the $X$, $Y$ and $Z$ passive mechanisms described in the preceding section. It is important to mention that for both the autonomous and the cooperative mode, the joint coordinates of the LIP joints — and therefore the components of vector $\mathbf{p}_\theta$ —, include the LIP joint displacements resulting from the human interaction and the LIP joint displacements resulting from the motion of the macro manipulator, which are respectively depicted by the $\mathbf{Z}_{h\theta}$ and *Passive dynamics* blocks in Fig. 4.7.

The main contribution of the outer loop control developed in this work is that it takes into account all inputs (human, environment, and desired trajectory) at all times. Indeed, the architecture of the controller remains unchanged regardless of the operation mode. However, parameters such as the gains can be modified in order to obtain a better performance or to cancel a certain input. The equation of the general controller, $C_o$, is as follows :

$$\begin{aligned} \dot{\mathbf{p}}_{ref} = \quad & \mathbf{K}_{Pt}\mathbf{e}_t + \mathbf{K}_{P\theta}\mathbf{e}_\theta + \mathbf{K}_D\dot{\mathbf{e}}_\theta + \mathbf{K}_F\mathbf{e}_f \\ & + \mathbf{K}_{NL}\mathbf{f}_{NL} \end{aligned} \tag{4.2}$$

where $\dot{\mathbf{p}}_{ref}$ is the commanded position vector of the end-effector of the macro manipulator fed to the inner controller described above, as shown in Fig. 4.7. Each of the terms of equation (4.2) favours a certain behaviour of the uMan system. They are described as follows :

• $\mathbf{K}_{Pt}\mathbf{e}_t$ :
The gain matrix $\mathbf{K}_{Pt}$ comprises the proportional gains that ensure that the desired trajectory is followed by the macro manipulator's end-effector (the macro-mini attachment point) whose position with respect to the fixed frame is noted $\mathbf{p}$. The error vector $\mathbf{e}_t = (\mathbf{p}_t - \mathbf{p})$ therefore includes the error between the desired macro manipulator position vector $\mathbf{p}_t$ and its actual position vector $\mathbf{p}$.

• $\mathbf{K}_{P\theta}\mathbf{e}_\theta$ :
The gain matrix $\mathbf{K}_{P\theta}$ comprises the proportional gains related to the displacements of the LIP joints relative to their equilibrium configuration. The error vector $\mathbf{e}_\theta = (\mathbf{p}^*_\theta - \mathbf{p}_\theta)$ therefore represents the error between the position of the end-effector of the mini manipulator relative to the end-effector of the macro manipulator corresponding to the equilibrium configuration,

noted $\mathbf{p}_\theta^*$ and the actual position vector of the end-effector of the mini manipulator relative to the macro manipulator, $\mathbf{p}_\theta$. As described in Section 4.2, the motion of each of the passive modules of the mini manipulator can be described as an equivalent pendulum motion, which yields

$$\mathbf{p}_\theta = \begin{bmatrix} l_x \sin\theta_x & l_y \sin\theta_y & l_z \sin\theta_z \end{bmatrix}^T$$

where $l_x$, $l_y$, and $l_z$ are the effective radii of curvature of each LIP joint and $\theta_x$, $\theta_y$, and $\theta_z$ are the equivalent angles of each LIP joint [1]. The equivalent LIP joint angles $\theta_x$, $\theta_y$, and $\theta_z$ are equal to zero when the LIP mechanisms are at their equilibrium configuration. Therefore, in order to maintain the manipulator still when it reaches its equilibrium configuration, the components of $\mathbf{p}_\theta^*$ are also equal to zero. For small angles, the relationship becomes quasi-linear, i.e., $\sin\theta \simeq \theta$, thereby ensuring an immediate response to small displacements of the end-effector which is required for fine manipulation.

• $\mathbf{K}_D\dot{\mathbf{e}}_\theta$ :

The gain matrix $\mathbf{K}_D$ comprises the derivative gains related to the velocity of the end-effector of the mini manipulator relative to the velocity of the end-effector of the macro manipulator. The error vector $\dot{\mathbf{e}}_\theta = (\dot{\mathbf{p}}_\theta^* - \dot{\mathbf{p}}_\theta)$ therefore includes the velocity of the end-effector of the mini manipulator relative to the macro manipulator, noted $\dot{\mathbf{p}}_\theta$, and the desired value of this velocity vector, noted $\dot{\mathbf{p}}_\theta^*$, which is equal to zero. This term mainly reduces the oscillations around the equilibrium configuration of the mini manipulator.

• $\mathbf{K}_F\mathbf{e}_f$ :

The gain matrix $\mathbf{K}_F$ comprises the gains associated with the filtered (low-pass) error vector $\mathbf{e}_\theta$ applied to the relative displacement of the mini manipulator with respect to the macro manipulator. This term stably increases the controller DC gain and adds virtual inertia and damping to the response. It makes the interaction more intuitive and comfortable for the operator when a high-force input is performed, which is directly related to a large LIP joint displacement due to the effect of gravity, such as a push-away motion. This virtual dynamics is not felt when an interaction or a sharp change of direction is initiated because of the gain vector $\mathbf{K}_{P\theta}$. Depending on the dynamics of the LIP joints (radius of curvature, weight, friction) this term might not be necessary.

• $\mathbf{K}_{NL}\mathbf{f}_{NL}$ :

The gain matrix $\mathbf{K}_{NL}$ comprises the gains that regulate the effect that the nonlinear functions $\mathbf{f}_{NL}$ have on the reference velocity $\dot{\mathbf{p}}_{ref}$. This nonlinear function should generate relatively larger response when the end-effector is near its physical boundaries in order to avoid any

1. The vertical parasitic motions induced by the horizontal motions ($x$ and $y$) are not considered in the evaluation of the vertical $z$-motion (Sarrus mechanism) since they can be shown to be negligible.

contact with mechanical limits and to counter the effect of gravity. For the uMan, in order to alleviate the partial payload that the human operator has to haul, the nonlinear functions for the horizontal LIP joints are related to the parasitic vertical motion of the pendulums such that

$$f_{NL}(\theta_x) = sign(e_{\theta x})\frac{x_{\theta z}}{x_{\theta znorm}}, \tag{4.3}$$

$$f_{NL}(\theta_y) = sign(e_{\theta y})\frac{y_{\theta z}}{y_{\theta znorm}}, \tag{4.4}$$

with

$$x_{\theta z} = l_x[1-\cos\theta_x], \tag{4.5}$$

$$y_{\theta z} = l_y[1-\cos\theta_y], \tag{4.6}$$

where $e_{\theta x}$ and $e_{\theta y}$ are the horizontal components of $\mathbf{e}_\theta$, and $x_{\theta znorm}$ and $y_{\theta znorm}$ are the heights at which it is desired to obtain $f_{NL}(\theta) = 1\ m/s$. It is recalled that the equivalent LIP joint angles $\theta_x$ and $\theta_y$ are equal to zero when the LIP mechanisms are at their equilibrium configuration. The effect of this nonlinear function (red dashed line) on the reference velocity is illustrated in Fig. 4.8. The linear function (blue dashed-dotted line) represents a component of the function $\mathbf{K}_{P\theta}(\mathbf{e}_\theta)$ — linear for small angles — and the combination of both corresponds to the black solid line. Larger angles are thus more penalized and thereby generate relatively larger responses. For the Sarrus mechanism, it was found that the nonlinear function is optional since

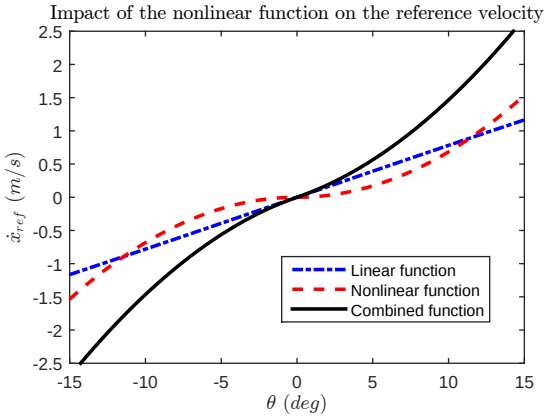


FIGURE 4.8 – The effect of adding a nonlinear function to the linear reference velocity output.

there is no pendulum effect and since the passive range of motion is large enough to prevent ever reaching the physical limits when loaded. Nevertheless, a nonlinear function should be added to the outer control law when the passive range of motion is small.

### 4.3.3 Stability analysis

Before implementing the control law it is important to assess the behaviour of each of the interaction parameters as well as their limit. Using a theoretical model, it is possible to obtain

a first estimate of the stable interval for the gain values $\mathbf{K}_P$, $\mathbf{K}_D$, $\mathbf{K}_F$, and $\mathbf{K}_{NL}$. A general guideline for the manual implementation and intuitiveness assessment is also deduced from this analysis. The dynamics of the end-effector for a single dof is based on the following pendulum equation, namely,

$$ml\ddot{\theta} = F\cos\theta - mg\sin\theta - m\ddot{p}\cos\theta \tag{4.7}$$

where $m$ is the payload value including the weight of the suspended part of the mini mechanism, $F$ is the horizontal human input force, $g$ is the gravitational acceleration, and $\ddot{p}$ is the macro robot acceleration.

From the dynamic equation (4.7) and the control law (4.2), a simulation is designed in order to represent the behaviour of the end-effector in the $x$-direction. The speed of the macro robot is limited to 1 m/s, the pendulum weight, $m$, is equal to 30 kg, and its effective length is equal to 0.6 m. The macro manipulator motion is also delayed by 0.15 second which is deduced from the real macro manipulator dynamics. This simulation provides a clear methodology for the evaluation of the highest stable gains for all parameters. More specifically, it was found that the gains have to be tuned in the following order : $\mathbf{K}_P$, $\mathbf{K}_{NL}$, $\mathbf{K}_D$, and then $\mathbf{K}_F$. The approach is defined as follows :
*i*) $K_P$, which yields a quick and immediate response, is first tuned to the highest stable gain with small damped oscillations,
*ii*) $K_{NL}$, which generates larger responses for larger mini displacements, is then tuned following the same criterion,
*iii*) $K_D$, which reduces the oscillations around the mini manipulator's rest position, is tuned to damp as much as possible the small oscillations,
*iv*) $K_F$, which stably increases the controller DC gain and introduces small virtual inertia and damping for push-away motion, is tuned to a stable gain that does not significantly slow down the settling time.

The stable boundaries found for each of the gains are : $K_P = [1.5;\ 7.5]$, $K_{NL} = [0;\ 0.6]$, $K_D = [0;\ 0.85]$, and $K_F = [0;\ 35]$. A simulation example of the resulting stable controller including the four cooperative gains is depicted in Fig. 4.9. Moreover, an unstable high gain response corresponding to each of the steps of the tuning procedure is illustrated in order to demonstrate that the final control law, in addition to being stable, has the highest DC gain response. It is important to note that these values are computed with a theoretical model and have to be adjusted afterwards with the real macro-mini manipulator using the same procedure.

### 4.3.4 Cooperative mode

When the cooperative mode is enabled, it is necessary to prescribe the positions of the macro manipulator as the desired trajectory position inputs $\mathbf{p}_t$ in order to obtain a pure pHRI. It is also possible to set the components of $\mathbf{K}_{Pt}$ equal to zero for redundancy purposes. With

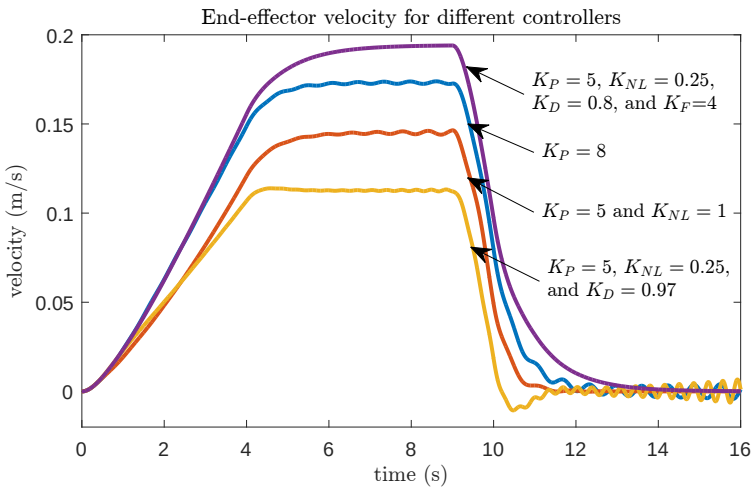


FIGURE 4.9 – Three unstable responses with partial control laws and high gain values, and a stable response with the proposed control law and adequate gain values. The input is a horizontal force on the end-effector going from 0 N to 10 N in 4 seconds followed by a constant 10 N input for 5 seconds which then ends by a force release to 0 N in 1 second.

this approach, the only input is then the LIP joint angles, i.e., the human and environment interactions. The equilibrium positions $\mathbf{p}_\theta^*$, $x_{\theta z}^*$, and $y_{\theta z}^*$ in cooperative mode for each LIP joint are acquired when the system is initialized and the mechanism is stationary. The same control parameter values are used when the uMan is loaded, apart from the equilibrium position $z_\theta^*$ for the vertical LIP joint (Sarrus mechanism) which is predefined depending on the payload to be handled. This procedure is necessary in order to take into account both states, namely the loaded and unloaded states.

### 4.3.5 Autonomous mode

When the autonomous mode is enabled, the desired trajectory position vector $\mathbf{p}_t$ is defined by the assisted trajectory generation and the components of $\mathbf{K}_{Pt} \neq 0$. The optimal approach to use this unique controller is to maintain the other terms active in the control law — which depend on the LIP joint angles — in order to stabilize the uMan as well as to react to external contacts. It is also advisable to keep the control parameter values used for the cooperative mode. Using this approach, the mode switch (autonomous to cooperative) for a physical human intervention — which is described in the next subsection — is smoother. However, this approach is only feasible if the autonomous trajectory does not produce high jerks. Indeed, high-frequency variations in the acceleration favour large oscillations of the LIP joints and thereby reduce the positioning accuracy and can even eventually trigger the collision detection. In a case where the planned trajectory generates high jerks, an easy solution would be to reduce all the parameter gains used for the autonomous mode such that $\mathbf{K}_{Pt}$ could be smaller. This approach can still lead to a precise positioning but slightly deteriorates the collision switching

smoothness, namely the switch from autonomous to cooperative. This mode switching issue thus justifies the development of an effective means of generating low jerk trajectories in order to fully exploit the potential of the underactuacted redundant manipulator.

### 4.3.6 Trajectory generation

In a context of pHRI, it is expected to have an adaptable autonomous trajectory motion. Indeed, it should be easy to program the desired trajectory, as well as the task to be performed, depending on the environment, and to be able to physically interrupt the robot motion at any time. Therefore, an effective trajectory should include many way points and the ability to be automatically replanned. A relevant approach in order to consider these issues is to use cubic splines (Bartels et al. [1987]). The cubic spline has the advantage of being continuous up to the third derivative and to be computationally efficient. On-line recomputing is thereby easier and the jerk, i.e., the time derivative of the acceleration, is thus continuous.

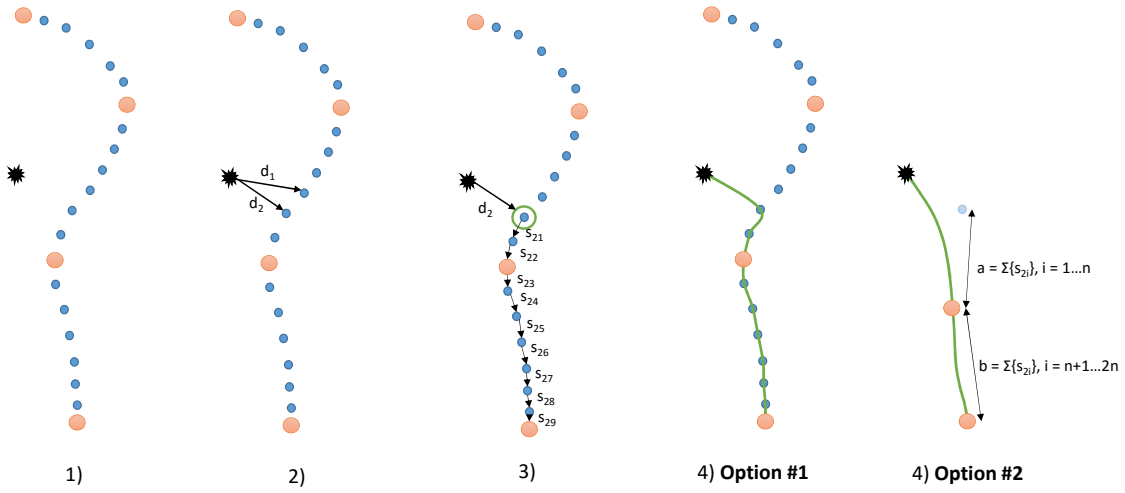


FIGURE 4.10 – Replanning algorithm : Steps to recompute the best trajectory using a cubic spline.

With the help of an intuitive user interface, the operator can physically teach the desired trajectory to the uMan by recording a set of main points. Depending on the total trajectory length, a time duration is associated with each segment between the main points. Then, a trajectory planning algorithm can be used. A simple choice in this case is to use an adapted version of the $A^*$ search algorithm (Hart et al. [1968]) in order to find the optimal set of points to reach the final destination. More specifically, the step-by-step algorithm is illustrated in Fig. 4.10 and described as follows :

1. Compute the entire trajectory from the desired starting position to the final destination

based on a cubic spline using the recorded main points. The resulting spline is composed of a list of way points.

2. Find the two way points that are the closest to the actual robot end-effector position using the Euclidean distance ($d_1$ and $d_2$).
3. From these two way points find the closest one relative to the final main point $n$ using the sum of each remaining sub segment $s_{xi}$ (with $\sum_{i=1}^{n} s_{1i}$ and $\sum_{i=1}^{n} s_{2i}$)
4. Compute the new trajectory with a cubic spline
   a) **Option #1** : using the remaining way points.
   b) **Option #2** : using new equidistant main points. These new main points are located on the initial spline but are equidistant from each other as well as from the starting way point. For instance, if there are only two remaining main points the total sum of each remaining sub segment is divided in two and the result redefines the new locations, as shown in Fig. 4.10. Note that the final main point is never relocated.

The first option leads to a more accurate trajectory but generates high jerks and high accelerations when launched close to the initial spline. It thereby requires the control parameter gains to be smaller in autonomous mode. On the other hand, the second option is slightly less accurate but allows more time to accelerate and yields smoother curves reducing the high jerks in the replanning.

### 4.3.7 Collision detection

In addition to its intuitiveness, one of the most important features of the uMan is its safe behaviour. Indeed, the LIP joints provide a very fast response to contacts but the macro manipulator still has to react accordingly when in autonomous motion. The proposed collision detection which is implemented in the uMan drastically improves the detection time for any disturbances in its planned trajectory and produces a smooth transition to the cooperative mode. Indeed, when a collision is detected, the autonomous parameter gain values transit linearly at a pre-defined rate to the cooperative parameter gain values. If the transition rate is too fast, it generates a large reaction force on the heavy macro manipulator which therefore disengages the joint safety clutches. On the other hand, if the transition rate is too slow the macro manipulator maintains its desired trajectory motion slightly longer which produces a larger angle at the LIP joint and generates a slingshot effect because of the control correction on the angle displacement. For the proposed manipulator and controller, it has been found heuristically in experimentation that a switching rate of 12 Hz is leading to the smoothest transition.

The algorithm that triggers the detection uses the equation of motion of a pendulum suspended to a moving cart, which yields, for a single degree of freedom,

$$0 = \ddot{x}\cos\theta + g\sin\theta + l\ddot{\theta} \tag{4.8}$$

where $\ddot{x}$ is the acceleration of the macro manipulator joint, $g$ is the gravitational acceleration, $l$ is the equivalent radius of curvature of the LIP joint, and $\theta$ and $\ddot{\theta}$ are respectively the LIP joint angle and angular acceleration. After linearization and simplification for small angles, the equation yields

$$0 = \ddot{x} + g\theta. \tag{4.9}$$

Considering that (4.9) is a simplification of (4.8) and that some inherent dynamics such as friction might be present, the proper way to use this equation is to transform it into the following inequality,

$$|\ddot{x} + g\theta| < c_{lim} \tag{4.10}$$

where $c_{lim}$ is the threshold to detect a contact with the LIP joint during an autonomous motion. This threshold is determined heuristically and should not trigger false collision detections in the autonomous mode but should be sensitive enough in order to detect light contacts. If the actual acceleration of the macro manipulator $\ddot{x}$ is too noisy, then the desired acceleration $\ddot{x}_t$ can be used but $c_{lim}$ should be adjusted accordingly, i.e, most probably increased.

It is a good practice to add redundancy when considering safety issues. This is why two other collision detection methods are implemented in the prototype. The first one limits the Cartesian acceleration of the LIP joints and the second one limits their displacement, yielding respectively

$$\ddot{\mathbf{p}}_\theta^T \ddot{\mathbf{p}}_\theta < a_{lim}^2 \tag{4.11}$$

$$(\mathbf{p}_\theta^* - \mathbf{p}_\theta)^T (\mathbf{p}_\theta^* - \mathbf{p}_\theta) < p_{lim}^2 \tag{4.12}$$

where $a_{lim}$ and $p_{lim}$ are respectively the thresholds on the acceleration and on the displacement of the mini manipulator with respect to the macro manipulator, which is directly related to the motion of the LIP joints. These methods can be slower to trigger the detection or even ineffective — as depicted in Section 4.4.1 — but they should nonetheless be integrated into the algorithm.

## 4.4 Experimental validation

Even though the capability of the active-passive architecture to minimize the impedance felt by the operator at the end-effector has been demonstrated in Labrecque et al. [2016], it is still necessary to assess the viability of the uMan regarding safety and effective fine manipulation. Therefore, the collision detection is investigated for safety, a peg-in-hole task is evaluated for fine manipulation, and two different assembly mock-up tasks are performed to quantitatively assess realistic physical human-robot interactions.

The control parameter values used for the uMan prototype presented in Section 4.2 and shown in Fig. 4.6 are given in appendix 4.7.1. The ranges of motion of the HIA and LIP joints are

also presented in appendix 4.7.1. A programmable logical controller (PLC) is used to manage the basic states and safety features of the gantry system such as limit switches and hardware faults. The control law (4.2) and its associated state machine are thereby implemented on top of this PLC using *RT-LAB* and *MATLAB/Simulink*. Only encoders are used as input and feedback sensors for the uMan control. However, two six-axis force/torque sensors can be appended at the end-effector for analysis purposes, depending on the task to be evaluated.

### 4.4.1 Collision detection validation

The first feature to be evaluated is the collision detection. It is important to implement the technique that will detect a collision as quickly as possible and that produces the smallest impact force. Moreover, it should be assessed in a standard pHRI industrial context by respecting the physical and psychological interaction limits recommended by previous works on the subject. For instance, in order to prevent any psychological trauma, the speed of the robot's end-effector should be limited to 0.6 $m/s$ in autonomous mode (Rahimi and Karwowski [1990]). Furthermore, it has been established in Yamada et al. [1997] that the static and dynamic tolerance contact force $F_c$ — with a minimum contact area of 0.0015 $m^2$ — is 50 $N$ for a human being.

First, the superiority of the contact index — based on (4.10) — using the pendulum-on-a-moving-cart dynamics is demonstrated in comparison to the other two methods — based respectively on (4.11) and (4.12) — proposed in Section 4.3.7, namely the acceleration index and the position index. The thresholds for the three different collision detections are summarized in table 4.1 for each LIP joint, i.e., each direction. The unloaded state allowing a smaller range of motion than the loaded state for the vertical LIP joint (Sarrus mechanism), it is thus required to have different position thresholds depending on whether or not a payload is grasped by the end-effector.

TABLE 4.1 – Thresholds for collision detection.

| Joints | $X$ | $Y$ | $Z$ |
|---|---|---|---|
| $c_{lim}(m/s^2)$ | 0.42 | 0.42 | 0.5 |
| $a_{lim}(m/s^2)$ | 0.5 | 0.5 | 1 |
| $p_{lim}(m)$ | 0.06 | 0.06 | unloaded : 0.01 ; loaded : 0.05 |

Fig. 4.11 shows a collision detection in the horizontal $Y$-direction using the acceleration index. The autonomous motion was set to reach a speed of 0.5 $m/s$ until the impact. In this case the contact index was inactive in order to show that the acceleration index could potentially lead to similar detection timing results. Indeed, with a small acceleration threshold $a_{lim}$ the collision detection can be quite fast but can be falsely triggered when higher autonomous accelerations are desired. For this reason, $a_{lim}$ is usually set above 0.7 $m/s^2$. However, the worst case, if there is only an acceleration index, would be a compliant collision unable to trigger the detection.

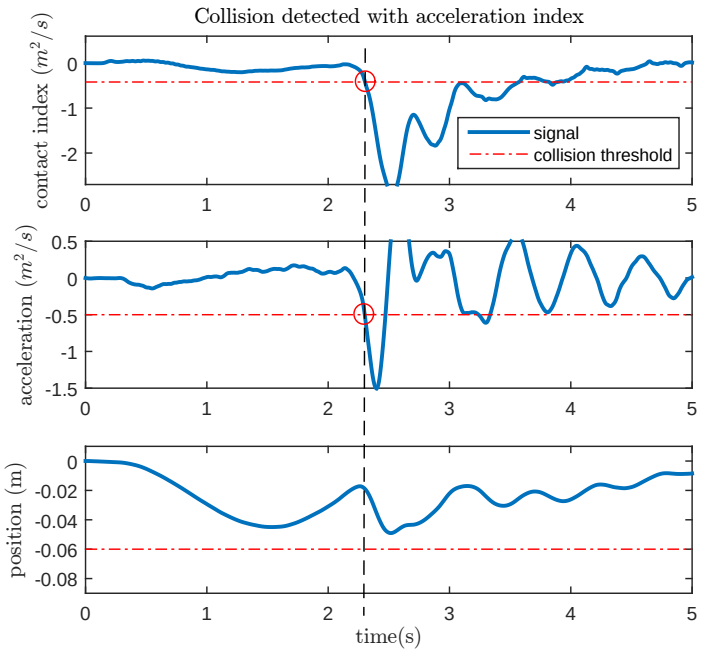


FIGURE 4.11 – Collision detected with the acceleration index (contact index inactive). The red circles identify the points where the thresholds are reached and the collision detection is triggered. In this case, the contact index and the acceleration index are reached at the same time, without triggering the position index.

This issue is demonstrated in Fig. 4.12 where the collision is detected by the position index but not the acceleration one. In this case, the inactive contact index detected the collision 0.5 $s$ earlier than the position index. The contact index detects on average a collision within 0.1 to 0.2 second depending on the manipulator velocity. The contact index is therefore faster to respond and more reliable than the two basic collision detections.

The enhanced safety provided by the collision detection is now discussed by considering the forces generated by a collision with two different surfaces, namely a static hard wooden surface and a compliant human hand. The robot's end-effector reaches a speed between 0.5 and 0.6 $m/s$ before it hits the surfaces. As expected, the collision with the rigid surface produces larger impact forces. However, the peak force is never above 30 $N$, as depicted in Fig. 4.13, and remains much smaller than the pain tolerance limit $F_c$ of 50 $N$. It is also interesting to see in Fig. 4.13 that a collision with an unconstrained human hand generates forces smaller than 10 $N$. The collision detection specially developed for the active-passive uMan leads to a safe shared human-robot workspace.

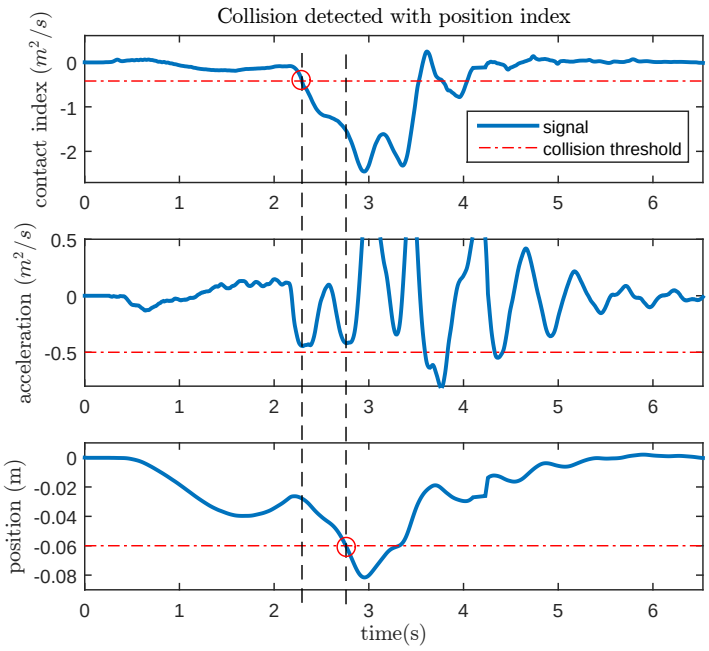


FIGURE 4.12 – Collision detected with the position index (contact index inactive). The red circles identify the points where the thresholds are reached and the collision detection is triggered. In this case, the contact index, if activated, would have triggered the collision detection before the position index, without triggering the acceleration index.

### 4.4.2 Peg-in-hole validation

The second feature to be assessed is the ease of fine manipulation and its resulting effectiveness. Unfortunately, the ease of manipulation is not a feature that can be directly measured like inertia and interaction forces. For this reason, a specific peg-in-hole task has been designed to assess the two main features that can be used to define the ease of manipulation, namely effort and intuitiveness. Using this specific peg-in-hole task, the uMan is compared to the state-of-the-art admittance control commonly used in pHRI (Lecours et al. [2012]). The set-up for the task consisted of a 4-hole rectangular pattern and a peg appended to the uMan's end-effector carrying a payload of 11.4 $kg$ (25 $lbs$) as illustrated in Fig. 4.14. The peg has a diameter of 25.70 $mm$ while the holes have a diameter of 26.00 $mm$. The admittance control is used with the three LIP joints completely locked and with the end-effector force/torque sensor as the operator inputs. A second force/torque sensor, mounted on the peg, is used to record the contact forces with the environment. The admittance parameter values used for this task are found heuristically in order to generate the fastest motions possible without producing unstable contacts ($m = 35\ kg$ and $c = 396\ Ns/m$ for the axis normal to the task surface).

Three tests were performed, namely, a 4-hole run in 30 seconds with the admittance control (as fast as possible), a 4-hole run in 30 seconds with the uMan (in order to match the admit-

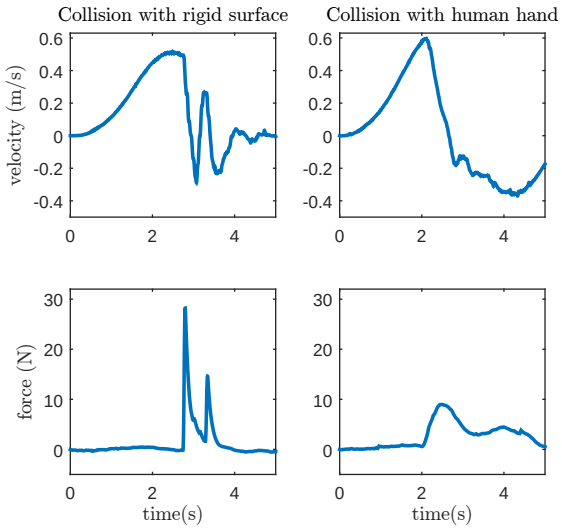


FIGURE 4.13 – Examples of the normal forces generated by collision of the uMan with different environments during an autonomous motion.

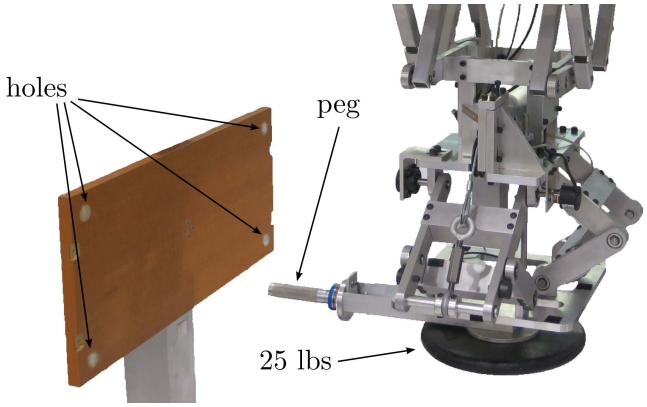


FIGURE 4.14 – Set-up for the peg-in-hole task.

tance execution time), and a 4-hole run in 14 seconds with the uMan (as fast as possible). The 30-second admittance and 30-second uMan runs are performed in order to compare the forces applied by the operator and generated on the environment with controlled speed and acceleration. This comparison gives a measure of the reduction of the human effort provided by the uMan, for a given task. The fast uMan run is then performed in order to compare — with the 30-second admittance run — the speed of execution and the required operator force to achieve similar environment forces. This comparison gives a measure of the improvement in the intuitiveness.

An example of the forces generated on the environment for a peg insertion and peg pull out during an admittance control and a 30-second uMan run is shown in Fig. 4.15. It can be observed that the 30-second uMan peg insertion force at about 0.8 second is approximately

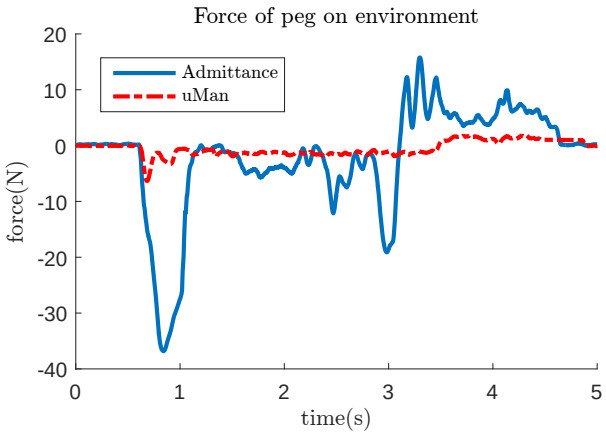


FIGURE 4.15 – Example of the normal forces generated on the rigid environment during the peg-in-hole task for the admittance control and the uMan for the 30-second tests.

four times smaller than the admittance control peg insertion force. This result is confirmed with the box plots shown in Fig. 4.16, representing two runs of each test, i.e., eight peg insertions.

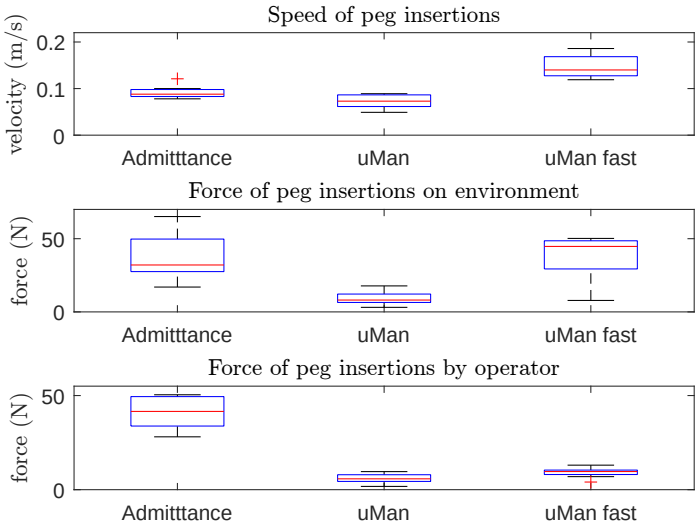


FIGURE 4.16 – Examples of the normal forces applied on the rigid environment during the peg-in-hole task for the admittance control and the uMan. The boxplots give the minimum, maximum, first quartile, third quartile, and median values for each test, including eight peg insertions.

Indeed, it is clear, from Fig. 4.15 and Fig. 4.16, that for the same execution speed, the uMan requires significantly smaller forces from the operator and produces smaller forces on the

environment. These results demonstrate that the exact same task can be executed with considerably less effort using the uMan than using the admittance control. It is also shown that the uMan can performed the peg insertion twice as fast as with the admittance control while generating similar forces on the environment but with smaller operator forces. The uMan's speed advantage, which also requires smaller operator forces than for the slower admittance control, demonstrates its superior intuitiveness. These conclusions are also true for the forces generated during peg pull outs, excepted that the fast uMan forces on the environment are much smaller (around 10 $N$).

Therefore, due to its resulting ease of manipulation, the macro-mini uMan enables fast and low-impedance interactions with constrained and unconstrained environments. As mentioned in the first part of this chapter, the main reasons for the effectiveness of the uMan is that its macro-mini architecture allows a complete decoupling of the dynamics of the robot and of the human operator, due to the redundant active (macro) and passive (mini) joints. With this architecture, all the work in the manipulative space is done by the human operator, therefore minimizing the mechanical impedance.

### 4.4.3 Assembly tasks validation

The last feature to be evaluated is the adaptability of the uMan to different industrial contexts. In order to demonstrate this feature, mock-ups of real assembly tasks were tested in the laboratory. A simple user interface, shown in Fig. 4.17, was also developed in order to provide an intuitive and adaptable communication channel and programming interface between the operator and the uMan.

Three simultaneous means of interaction were possible with the uMan : a physical interaction with the end-effector, a remote controller attached to the end-effector, and a graphical user interface (GUI) on a computer screen. The physical interaction provided the cooperative motion, the collision detection, and the automatic return trigger. The remote controller was directly linked to the GUI and included a button for each feature present in the GUI.

The first mock-up validation is a trunk deck lid attachment application (deck lid : 11.2 $kg$). A picture of the interaction is presented in Fig. 4.18. A specific state machine, shown in Fig. 4.19, is designed in order to cover all aspects of a practical deck lid attachment task.

Using a physical interaction with the uMan, the operator has to define the pick-up, place-down, and certain way point locations for the autonomous trajectory. The autonomous mode is then launched, i.e., the robot fetches the first deck lid. Once the first deck lid has reached the operator's workstation, a screwing task is performed in cooperation with the uMan in order to maintain the deck lid in place. The uMan is then sent back to fetch the second deck lid while the operator is finishing the first deck lid installation. A collision and a hands-on-payload interaction is then performed with the second deck lid in order to complete the

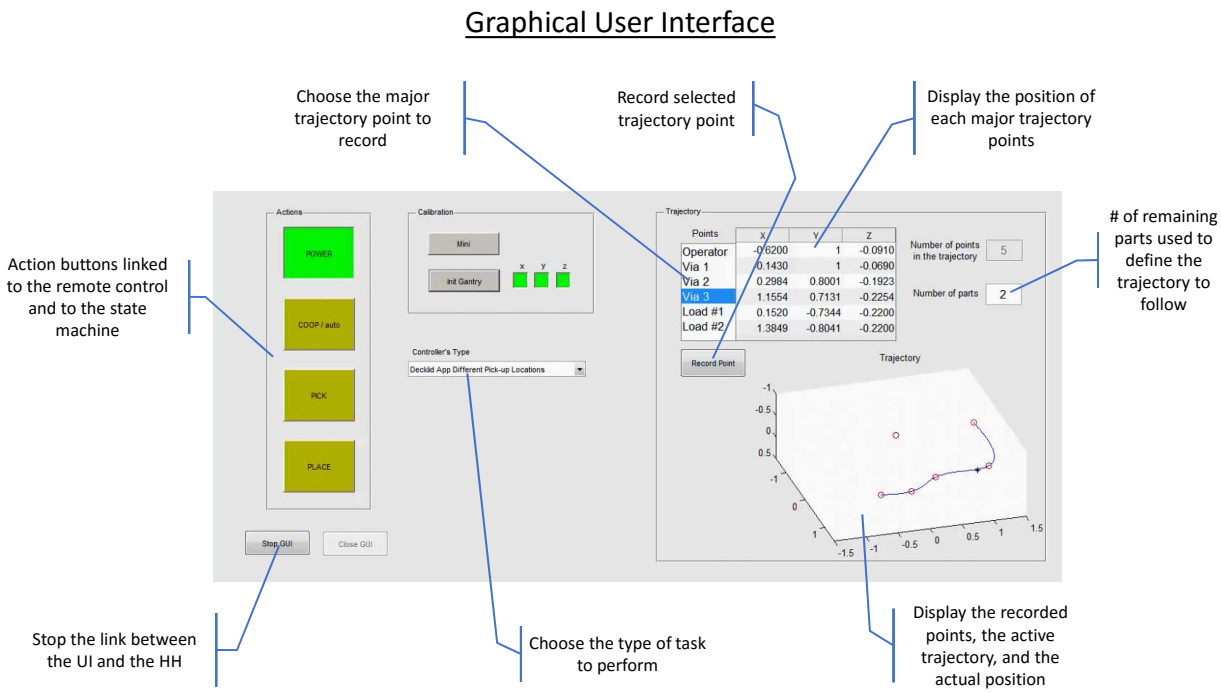


FIGURE 4.17 – Graphical user interface specifically designed for the uMan.

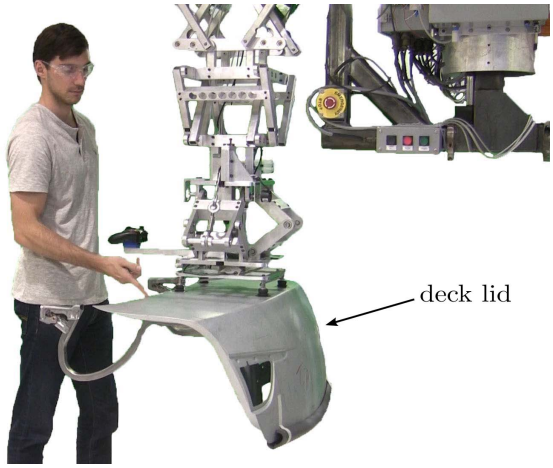


FIGURE 4.18 – Laboratory set-up used to emulate the assembly of a deck lid on a vehicle.

planned trajectory with a physical human-robot cooperation. In short, this task involves a simple trajectory/task teaching, an autonomous motion towards the part and towards the operator working zone, an autonomous part pick-up, a cooperative motion, a cooperative screwing task, and a collision detection.

The deck lid demonstration assessed the capabilities of the uMan to operate safely in the same workspace as a human being and to improve the operator's efficiency while reducing the

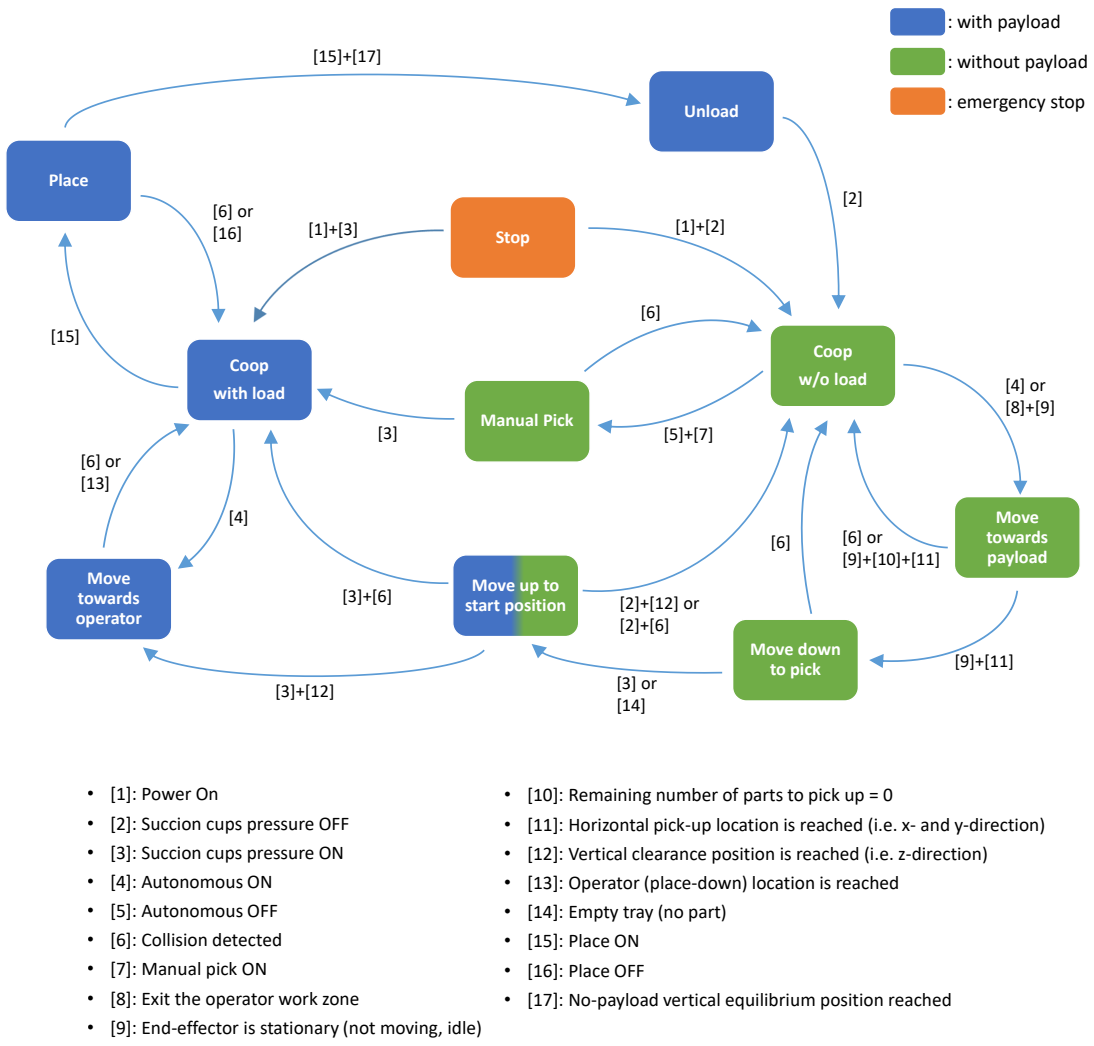


FIGURE 4.19 – State machine diagram for the deck lid application.

required physical efforts. In particular, the low impedance interaction makes the adjustment and screwing task much easier than with an admittance controller because of the natural and intuitive response of the uMan to the operators fine motions.

The second validation is a mock-up battery insertion application (mock-up battery : 10 $kg$). A picture of the interaction is presented in Fig. 4.20.

In this validation, the operator has to pick up the mock-up battery with an off-centred end-effector using a physical human-robot interaction. Once the battery is picked up, the operator has to perform a tight in-and-out insertion task that is not feasible without the assistance of the uMan. In short, this task involves a cooperative pick and place, a cooperative precise positioning, and a demonstration of the stability in the presence of rigid contacts as well as

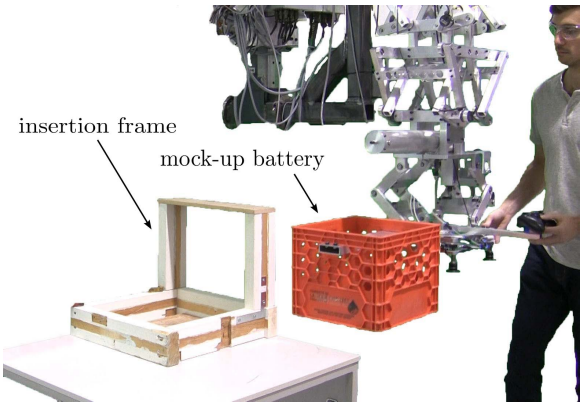


FIGURE 4.20 – Laboratory set-up used to emulate the insertion of a battery in the tight housing of a vehicle.

the direct environment feedback to the operator.

The mock-up battery insertion application assessed the capabilities of the uMan to enable cooperative fine manipulations with an off-centred payload and to allow hard contacts with any environment. The direct feedback to the operator of the contacts with the environment is provided by the low-impedance mini manipulator and yields a very stable and intuitive interaction.

## 4.5 Video demonstrations

Four videos showing the different experimental validations are available at

*http://robot.gmc.ulaval.ca/publications/these-de-doctorat*

The collision detection video demonstrates the impacts with the rigid surface and with the human hand, as well as different interferences during autonomous motion (*Chap4_ Collisions.mp4*). The peg-in-hole video shows the speed advantage of the uMan over the admittance control (*Chap4_ Peg_ in_ Hole.mp4*). The deck lid video shows the trajectory recording with the user interface as well as the execution of the mixed autonomous/collaborative deck lid installation(*Chap4_ Decklids.mp4*). Finally, the battery video demonstrates the tight insertion task, the stable bilateral contacts and the direct feedback using the mock-up battery (*Chap4_ Battery.mp4*).

## 4.6 Conclusion

This chapter introduced a novel underactuated macro-mini architecture adapted for pHRI in an industrial context, namely the uMan (underactuated manipulator). The mechanical design and the resulting advantages of the low-impedance passive joints ($X$, $Y$ and $Z$ motion) were described in detail. The advanced control of the uMan was then presented together with the

recommended approach for the trajectory planning and the new dynamics-dependent collision detection. The results of the experimental validations were then presented and discussed in order to demonstrate that the concepts developed in this work provide low-impedance physical interaction, which yields a very intuitive and effective manipulation environment as well as a safe cooperative workspace. Considering these positive results, the uMan is believed to have the potential to lead to effective architectures of robotic assistants.

## 4.7 Appendix

### 4.7.1 uMan parameters

The filter used for the error signal $e_f$ in equation (4.2) is a first-order low-pass filter with a cutoff frequency of 0.318 $Hz$. It is also important to reiterate that for the cooperative mode the diagonal components of the gain matrix $\mathbf{K}_{Pt}$ were set to zero for redundancy in the algorithm, although this is not mandatory.

TABLE 4.2 – Control parameters.

| Joints | $X$ | $Y$ | $Z$ |
|---|---|---|---|
| $K_{Pt}$ | 7 | 7 | 7 |
| $K_{P\theta}$ | 5 | 7.5 | 4 |
| $K_D$ | 1 | 1 | 0 |
| $K_F$ | 4 | 0 | 1 |
| $K_{NL}$ | 0.25 | 0.5 | 0 |
| $l$ | 0.6 | 0.6 | 0.2848 |
| $x_{\theta znorm}$ | 0.008 | 0.008 | – |

TABLE 4.3 – Range of motion.

| Joints | $X$ | $Y$ | $Z$ |
|---|---|---|---|
| $HIA(m)$ | 3.30 | 2.15 | 0.52 |
| $LIP(m)$ | 0.190 | 0.190 | unloaded : 0.036 ; loaded : 0.100 |

### 4.7.2 Validation of the low effective impedance using the first prototype

It is desired to obtain a robotic manipulator that can effectively follow a human being's interaction capabilities. To this end, it is required to reduce the control delay — if not eliminate it completely — and to respond quickly to high frequency inputs whatever payload the robot carries. In order to assess the effectiveness of the macro-mini (active-passive) mechanism proposed in this work, some preliminary tests were performed to compare the first prototype of the proposed architecture to a fully actuated robot using the state-of-the-art admittance control with optimal parameters.

### Test-Bench Design

In order to fairly compare both architectures, during the experimentation, the mini component is always appended to the macro manipulator, however the passive joints are locked for the fully actuated experiment. Using this approach, the prototype keeps the same weight and interaction set-up for both experiments which minimizes the undesirable experimental variations. The mini component of the prototype, attached to a 3-dof actuated gantry system, is shown in figure 4.21 with an example of a passive motion, and the complete macro-mini manipulator is shown in figure 4.22.


FIGURE 4.21 – LIP (mini) component of the macro-mini robotic manipulator attached to a 3-dof gantry structure (macro, not shown here). This architecture allows the $x$ and $y$ horizontal motions.

The mini component includes two identical four-bar passive parallelogram structures mounted orthogonally in series and each generating a pendulum dynamics. The length of the vertical bars are designed to be long enough in order to obtain a large radius of curvature, here 35.5 $cm$, and thereby, to emulate horizontal motions in $x$ and $y$. The nonlinear parasitic $z$-motion (vertical motion) due to the pendulum-type architecture generates a vertical force, which increases with the motion angle and the payload weight, and that passively brings the end-effector back to its equilibrium configuration. However, this return force also acts against the operator's ease of motion for large displacements. Indeed, the parasitic $z$-motion increases with the pendulum angle, which in turn increases the fraction of the weight of the payload that the operator has to support. To counter this effect, the nonlinear function for the macro-mini controller is chosen as

$$f_{NL}(\Delta z) = \text{sign}(\Delta x) k_z \Delta z \tag{4.13}$$

with

$$\Delta z = l[1 - \cos(\Delta\theta)] \tag{4.14}$$

where $k_z$ is a gain used to modulate the compensation on the horizontal motions proportionally to the $z$-displacement of the end-effector, $\Delta z$. Parameter $l$ is the radius of curvature of the

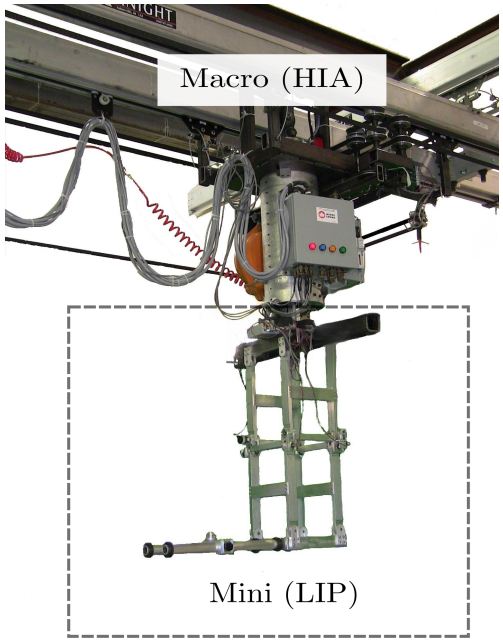


FIGURE 4.22 – Macro-mini manipulator. Macro : 3-dof gantry manipulator. Mini : 2-dof passive mechanism (horizontal motions).

pendulum and $\Delta\theta$ is the angle produced by the pendulum's displacement from its equilibrium point. For both horizontal motions, namely $x$ and $y$, the corresponding angle is read by an encoder located at a rotational joint on each parallelogram. A 6-dof force/torque sensor is also mounted between the operator handle and the end-effector in order to read the applied forces. Conveniently, the handle can also support a variety of payloads.

When the passive joints are locked, for the macro-only version of the robot, the force/torque sensor is used to measure the operator's input force and control the macro manipulator. Therefore, the admittance control described in section 4.3 is used in that case (it is recalled that the force/torque sensor is not used for control purposes in the macro-mini version of the robot). In order to obtain the lowest possible impedance, the smallest parameters, $m$ and $c$, that generate stable interactions, have been found heuristically for that specific experimental set-up.

Each passive parallelogram has a mass of approximatively 9 $kg$. Therefore, the mini component of the robot has a total mass of 18 $kg$ while the high-inertia macro has an equivalent moving mass of 500 $kg$ in the direction of $x$-axis and 350 $kg$ in the direction of $y$-axis. [2] The control parameters for the macro-mini manipulator are

$$k_P = 6,\ k_D = 1.5,\ k_z = 0.1,\ \text{and}\ l = 0.355\ m,$$

2. The macro component of the manipulator was designed for large payloads. Its architecture is described in detail in Gosselin et al. [2013].

while for the macro-only manipulator the selected parameters are

$$m = 35\ kg \text{ and } c = 80\ Ns/m.$$

It is also important to mention that a payload of 16 $kg$ (35 $lbs$) was mounted on the handle for the experimentation, leading to a total moving mass of 384 $kg$ in the $y$-axis. The desired inertia reduction is thus more than 10 times the actual inertia making the chosen admittance parameters in fact quite low for such a system, but still optimal for this experimental set-up.

**Results and discussion**

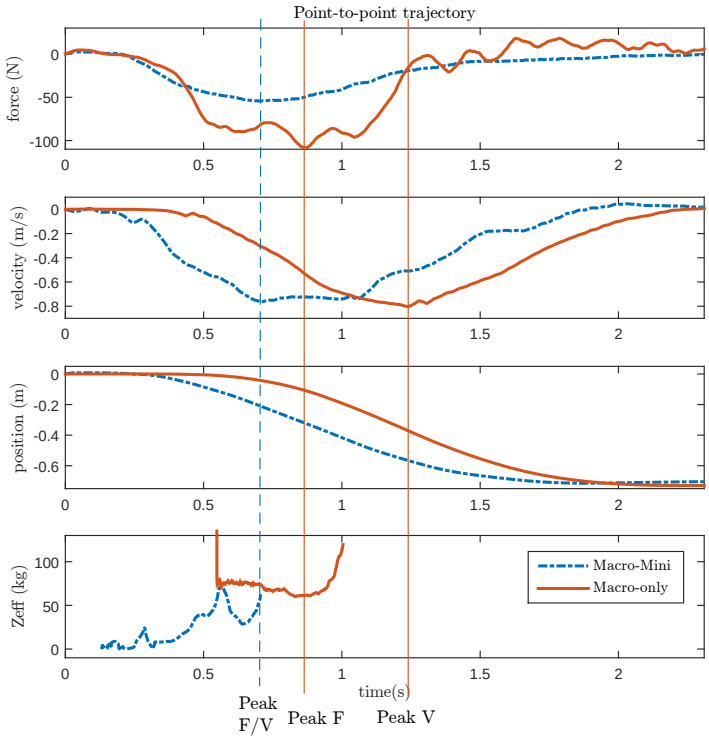


FIGURE 4.23 – Force, velocity and position responses, and effective impedance felt by the operator during the acceleration phase for the point-to-point task with the macro-mini (in dashed blue) and the macro-only manipulator (in solid red). Peak F and Peak V represent respectively the peak force and velocity of each manipulator.

The preliminary tests that were conducted to assess the performance of the macro-mini architecture are simple point-to-point tasks for which the input force, the velocity and position of the payload, and the effective impedance felt by the operator are studied. Example experimental results for a 0.7 $m$ linear displacement in the direction of the $y$-axis of the robot are shown in figure 4.23. The results for the macro-mini manipulator are represented by blue dashed lines, while the results for the macro-only manipulator are represented by red solid lines. For this specific task, the operator had to bring the payload to the 0.7 $m$ target as fast as

possible with a velocity limit of 0.8 $m/s$ of the active joint of the macro. Several improvements can be noticed with the macro-mini robot in comparison to the macro-only robot. The first important benefit is the absence of delay in the response. Indeed, it can be observed that, for the macro-mini robot, the motion is engaged immediately when an input force is applied to the system (at about 0.2 $s$), whereas the macro-only robot induces a delay of approximately 0.3 $s$. This delay can be easily observed when considering the elapsed time between the peak force ($Peak\ F$) and the peak velocity ($Peak\ V$) of each response, as indicated in Figure 8. Indeed, it can be observed that the peak force and the peak velocity coincide in the case of the macro-mini robot while the peaks are separated by a delay of 0.3 $s$ in the case of the macro-only robot. This delay is clearly perceptible by the operator and makes the interaction significantly less intuitive (the operator feels that they are dragging the robot). In both cases the velocity constraint was reached, but the macro-mini plateaued for a period of 0.4 $s$ which means that it could have fulfilled the task even faster considering the exact same input force if the velocity limitation had been higher. Actually, the amount of force required to attain the peak velocity is also a strong positive for the low-impedance interaction achieved with the passive system. Effectively, the necessary force to achieve 0.8 $m/s$ was approximately 50 $N$ for the macro-mini while it was required to apply twice the force for the macro-only robot (approximately 100 $N$). This result can be a major issue for pHRI, regarding safety, efficiency, and ergonomic considerations.

Another well-known problem in pHRI can be observed on the input force graph where a tight virtual mass reduction can generate an unstable behaviour. Here, for the macro-only robot, the high impedance of the macro mechanism combined with the stiff dynamics of the interaction apparatus (force/torque sensor, payload, parallel bars) produces an oscillating force input that requires higher admittance parameters in order to be filtered. Failing to do so would lead to discomfort for the operator or simply to an uncontrollable interaction. In order to further compare the two manipulator architectures, the effective impedance felt by the operator during the acceleration phase is plotted in figure 4.23. Here, the effective impedance is computed as an effective inertia, as follows

$$Z_{eff} = m_{eff} = f/a; \tag{4.15}$$

where $f$ is the force applied by the operator and $a$ is the acceleration of the end-effector. Obviously, in the portion of the trajectory where the acceleration is close to zero, the computed effective impedance becomes too large to be significant. The effective impedance is therefore not shown on the graph for these portions of the trajectory. For the macro-only manipulator with the optimal admittance parameters, the impedance felt is extremely high before the end of the delay and then it is quasi-constant between 60 to 76 $kg$. The macro-mini leads to a lower effective admittance, namely a short peak at 24 $kg$ — which roughly corresponds to the passive mechanism plus payload weight ($16 + 9 = 25\ kg$) — is observed before the end of the slight delay. The impedance then drops to 8 $kg$, and then slowly increases, due to gravity, to an effective impedance peak at around 70 $kg$ that directly implies that the limit of the range

of motion of the passive mechanism is reached. Indeed, this inertia is close to the limit in impedance reduction achieved by the macro-only manipulator.

In summary, the macro-mini mechanism eliminates the inherent delay, requires less than half the force to achieve the same velocity, generates a more stable interaction, and reduces considerably the effective impedance during the acceleration phase. Results obtained with other trajectories confirm the above observations.

### 4.7.3 Video demonstration

The accompanying video demonstrates the effectiveness of the macro-mini robotic manipulator (*Annexe_ Chap4_ Low_ Impedance.mp4*). The first part shows the intuitive interaction with the robot for large and fine motions without any payload, followed by an interaction with a 16 $kg$ (35 $lbs$) payload. The fast point-to-point task is then presented for both the macro-mini and the macro-only mechanisms with the 16 $kg$ payload. The video is available at

*http://robot.gmc.ulaval.ca/publications/these-de-doctorat*